NTU Journal of Renewable Energy (2026) Vol. 11 (1): 24-38
DOI: https://doi.org/10.56286/34rcgz95

IRAQI Academic Scientific Journals

ISSN: 2788-9912 (print); 2788-9920 (online)
NTU Journal of Renewable Energy
Available online at:
https://journals.ntu.edu.iq/index.php/NTU-JRE



Thermal Performance of Hybrid Pin-Fin/Metal Foam Heat Sinks: Toward Enhanced Cooling of Power Electronics in Renewable Energy Applications

Dina S. Ghasoob[1], Ayad S. Abedalh[1], Ali S. Muhsan[2]

[1]Engineering Technical College of Mosul, Northern Technical University, Cultural Group Street, Mosul, Iraq.
[2]Universiti Teknologi PETRONAS, Kampar, Perak, Malaysia.

Article Information

Received: 10 – April – 2026
Received in Revised form: 08-July-2026
Accepted: 15 – July - 2026
Published: 29 – July – 2026

Corresponding Author:
Ayad S. Abedalh

Email:
ayad.selman@ntu.edu.iq

Key words:
Hybrid heat sink; Metal foam; Pin-fin; Forced convection; Flow bypass; Electronic cooling.

ABSTRACT

This study experimentally investigates the steady-state and transient thermal performance of hybrid heat sinks under forced convection. The hybrid configurations consist of aluminum pin fins encapsulated with open-cell copper metal foam (90% porosity). A total of 24 independent experimental trials were conducted to assess a parametric matrix comprising two pin-fin outer diameters (10 mm and 15 mm), two inlet air velocities (0.75 m/s and 1.5 m/s), and three thermal power levels (20, 40, and 60 W). The maximum combined uncertainty for the temperature difference was ±1 °C. Findings reveal a strong geometry-dependent thermal behavior. The foam encapsulation of the compact 10 mm series consistently improved cooling, achieving a maximum thermal enhancement ratio of 22.5% over the bare baseline. Conversely, the extended 15 mm series induced a macro-scale flow bypass, resulting in a thermal degradation of up to −24.6%. Doubling the inlet velocity yielded cooling rate improvements of up to 29.4% for the 10 mm hybrid design. Ultimately, while the introduction of the highly conductive copper foam enhances the effective thermal conductivity of the fins, its application must be carefully scaled with the fin diameter to prevent severe aerodynamic blockage and subsequent thermal penalties.

© THIS IS AN OPEN ACCESS ARTICLE UNDER THE CC BY LICENSE :
https://creativecommons.org/licenses/by/4.0/

Introduction

Microelectronic devices have to shrink further because of the growing demand for more functions in limited space as well as for greater component density. With the shrinking dimension of these devices, their volumetric power dissipation has increased and the chances of hot spots forming are also greater. The reliability and lifetime of a device are reduced by solid-state degradation mechanisms (e.g. electromigration, thermally activated void nucleation or growth of intermetallic compounds) caused by operating at temperatures regularly in excess of design values [1–3]. In this way, thermal management has evolved from a secondary engineering consideration to a rate-limiting design constraint in almost all modern electronic platforms.

Conventional passive metallic heat sink designs are approaching their theoretical performance limits. With increasing applied heat flux densities, the plain fin arrays fail to maintain sufficiently low junction-to-ambient temperature differences, a fact pointed out in recent benchmarking studies [4],[5]. According to Swetha et al. [6], further quantification of this ceiling effect was made in a review of passive technologies, therefore necessitating the shift towards active or hybrid cooling architectures.

Active forced convection can overcome the basic drawback of passive systems owing to the mechanical replenishment of the thermal boundary layer at the fin–fluid interface which greatly reduces local convective resistance [7, 8]. Various experimental and computational studies have shown that an increase in Reynolds number leads to a proportional increase in the overall heat transfer coefficient [9],[10]. Despite this, an adequate increase in convective augmentation using velocity increase alone imposes significant aerodynamic penalties, including increased fan power and noise. Thus, a joint search for geometric solutions with high convective heat transfer area per unit volume is warranted.

Incorporating extended surfaces is a simple way to increase area. A study by Bunjaku et al. [11] showed that intentionally designed fin cross-sections can significantly increase convective throughput as compared to regular prismatic geometries. More recent research has focused on perforated and patterned pin-fin topologies; Zohora et al. [12] and Sahu et al. [13] reported an appreciable gain in heat transfer (enhancing the Nusselt number by up to 70.2%) due to flow agitation by jets created by perforation. As the fin density increases, the blockage of the inter-fin channels can reverse any area benefits by increasing the frictional pressure drop and the corresponding pumping power [14, 15]. Open-cell metallic foam offers an alternative paradigm, aiming to simultaneously maximize the surface-area-to-volume ratio, tortuous-path flow mixing, and skeletal thermal conductivity. Research by Singh et al. [16] and Kim et al. [17] reports considerable improvement in the convective heat transfer (enhancing the heat transfer coefficient by up to 532%) in jet impingement and pool boiling configurations, respectively. Foams are expected to have optimum morphologies in the porosity range of 0.79−0.95 and a pore density of 10−20 PPI, which offer good thermal conductance as well as fluid permeability [18, 19]. For porous materials, flow resistance capacity is important, but they show friction factors that are much larger than those for open channels as noted by Torres-Madroñero et al. [20].

The fact that neither solid fins nor metal foams alone can fulfill the multi-objective requirements of high heat dissipation and low pressure penalty motivated the development of hybrid architectures. Moghadam et al. [21] and Ghaleh et al. [22] reported enhancement in heat transfer of solid-porous composite fins. Raje and Dhiman [23] and Issah et al. [24] demonstrated the importance of optimizing the pore configuration parameters of hybrid systems. A feasible method to reduce pressure drop is partial foam filling [25], while the literature critiques the effectiveness of the bypass-channel [26],[27]. It has also been noted by the modeling community that thermal non-equilibrium effects inside the porous medium give rise to systematic errors when a conventional single-phase approach is employed.

Despite these combined advances, a significant knowledge gap remains regarding the mechanistic linkage between the geometric scaling of the fin array, the porous sheath morphology, and macro-scale flow bypass under representative operating conditions. While previous studies (e.g., [21-24]) demonstrated the general benefits of solid-porous composite fins, they primarily focused on steady-state conditions and lacked a systematic evaluation of the geometric threshold that causes performance inversion.

Therefore, the novelty of the present study lies in two main aspects compared to previous works: First, it systematically isolates the effect of fin outer diameter on inter-fin aerodynamic resistance to quantify the exact transition point from thermal enhancement to degradation (the bypass effect) in hybrid heat sinks. Second, unlike most existing literature that is limited to steady-state analysis, this study uniquely characterizes the transient thermal

inertia behavior governing the electronics' response to time-varying power profiles. By bridging these gaps, this comprehensive experimental study of hybrid aluminum/copper-foam pin-fin heat sinks under forced convection aims to identify the geometry threshold beyond which foam integration becomes harmful, providing critical design guidelines for practical applications.

2. Experimental Setup and Methodology

2.1. Wind Tunnel Facility and Airflow Control

All experiments were conducted in a specially designed horizontal open-circuit wind tunnel which imposes well defined forced convection conditions over the heat sink test section, as shown in Fig. 1. The tunnel housing, made of a 10 mm thick transparent plexiglass plate, allowed visual inspection of the test section. The test canal had a rectangular cross-section measuring 800 mm long, 105 mm wide and 50 mm high. The required airflow was generated by a centrifugal blower placed at the tunnel inlet and a variable autotransformer in the blower circuit facilitated continuous adjustment of fan rotational speed. The nominal inlet air velocities in the speed test were set at 0.75 m/s and 1.5 m/s. An MT-4615 digital anemometer was used to constantly check the actual velocity at the exit of the channel in order to ensure stable flow-field throughout every test.

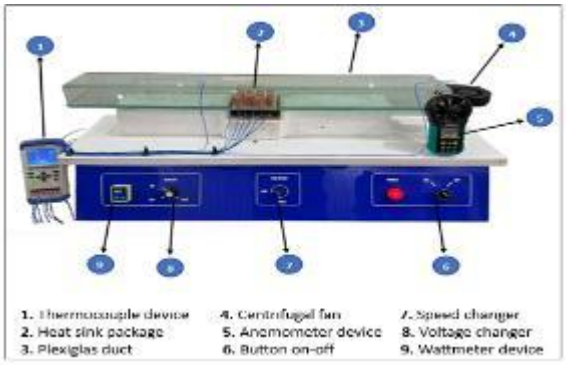


Fig. 1. Main components of the experimental wind tunnel assembly.

Thermal energy was introduced via a 100 mm × 100 mm × 5 mm resistive heater fabricated from stainless steel with a rated maximum power of 300 W (Fig. 2). A thermally matched copper spreader plate of identical planform dimensions was mounted directly above the heater to homogenize the heat flux. Thermal Grizzly Kryonaut interface material (k = 12.5 W/m·K) was applied at both the heater–spreader and spreader–heat sink interfaces to minimize contact resistance. To enforce a predominantly one-dimensional upward heat flux, the complete heating assembly was embedded within a precision-machined cavity in a thermostone insulation block featuring a 70 mm base thickness, as shown in Figs. 3 and 4. The air velocity was deliberately measured at the exit of the test section rather than the inlet. This approach ensures that the anemometer probe does not disturb the upstream flow profile or induce artificial turbulence before the air engages with the heat sink array. Given the closed-duct configuration, the principle of mass conservation ensures that the exit measurement accurately reflects the bulk flow rate traversing the test section.



Fig. 2. Centrifugal fan assembly utilized for controlled airflow delivery.



Fig. 3. Stainless steel heating element used as the primary thermal source.

The copper base plate was drilled with blind holes at regular spacings of 16.6 mm to accommodate five Type-K thermocouples to facilitate temperature acquisition across the heat sink footprint. A sixth and a seventh thermocouple were placed near the blower intake to record the undisturbed ambient temperature and at the channel exit to record the bulk outlet air temperature, respectively. The AT-4208 eight-channel digital data logger has been used for acquisition of all

thermocouple signals at a sampling interval of five seconds as shown in Fig. 5.

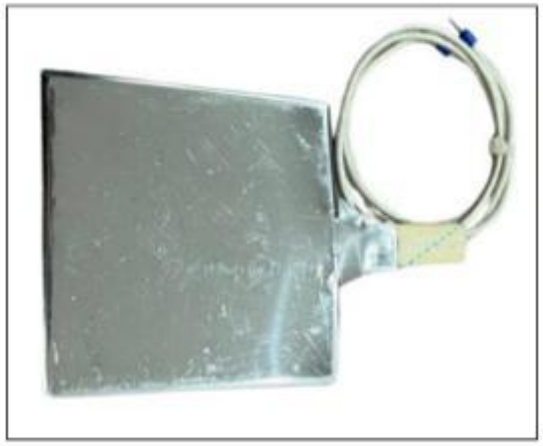


Fig. 4. Precision-machined thermostone insulation block with a recessed heating cavity.



Fig. 5. Multi-channel digital data logger interfaced with the thermocouple-embedded copper base plate.

The experimental procedure was based on a transient cooling cycle. Under each operating condition, the heater was turned on and allowed to develop into steady state, defined as the condition in which the temperature variation in all the base thermocouples remained within ±0.1 °C for a sustained period of time of at least 10 minutes.

Base temperatures, at which the steady states were nominally reached, were approximately 50 °C, 80 °C, and 130 °C for applied powers of 20 W, 40 W, and 60 W. To ensure a fully developed hydrodynamic flow before reaching the test section, an unheated entry length of 600 mm (approximately 8.5 times the hydraulic diameter of the channel) was provided. The flow regimes tested correspond to channel Reynolds numbers (*Re*) ranging from approximately 3,500 to 7,000, indicating transitional to turbulent flow conditions. Furthermore, the use of a 5 mm thick highly conductive copper spreader plate directly above the heating element ensured a uniform heat flux boundary condition at the base of the heat sink, mitigating localized hot spots.

2.2. Heat Sink Configurations

To enable a controlled parametric assessment of fin outer diameter and foam porosity, four unique heat sink designs were fabricated. Each of the specimens was made up of a common aluminum 6061 alloy base plate with dimensions 100 mm × 100 mm × 10 mm. The experimental matrix was designed on top of two geometric families: one compact series with nominal external fin diameter D = 10 mm and fin height H = 20 mm; and another extended series with D = 15 mm and H = 30 mm.

The baseline reference for each geometry was a bare aluminum pin-fin heat sink (PFHS). The baseline of the 10 mm series consisted of 23 cylindrical pins arranged in a staggered row pattern of 5-4-5-4-5. By contrast, the baseline of the 15 mm series was made up of 14 pins in a staggered layout of 4-3-4-3. The hybrid configurations (PFHS-MF) entailed encasing each aluminum pin in an annular copper foam sleeve. The structure had core-shell geometry.

The aluminum core was reduced to 5 mm in the case of the series of 10 mm and a sleeve of copper foam, with a thickness of 2.5 mm, was press-fitted over the core to recover the external diameter of 10 mm. The same process resulted in a 7.5 mm aluminum core for the 15 mm series. To provide a comprehensive geometric description, detailed top-view schematics of the heat sink arrays are presented in Fig. 6.

As illustrated, the 10 mm series feature a uniform longitudinal and transverse pitch of 20 mm. In contrast, the 15 mm series utilize a pitch of 23 mm and 27 mm to accommodate the larger fin diameters. These schematics explicitly detail the staggered layouts, the inter-fin spacing, and the exact dimensions of both the solid aluminum cores and the outer porous sleeves. Precision machined foam tubes that are made from open-cell copper foam sheets with 90% porosity are made at 40 PPI pore density with exact interference-fit dimensions to ensure intimate metal to metal contact at the core-shell interface (see Fig. 7)

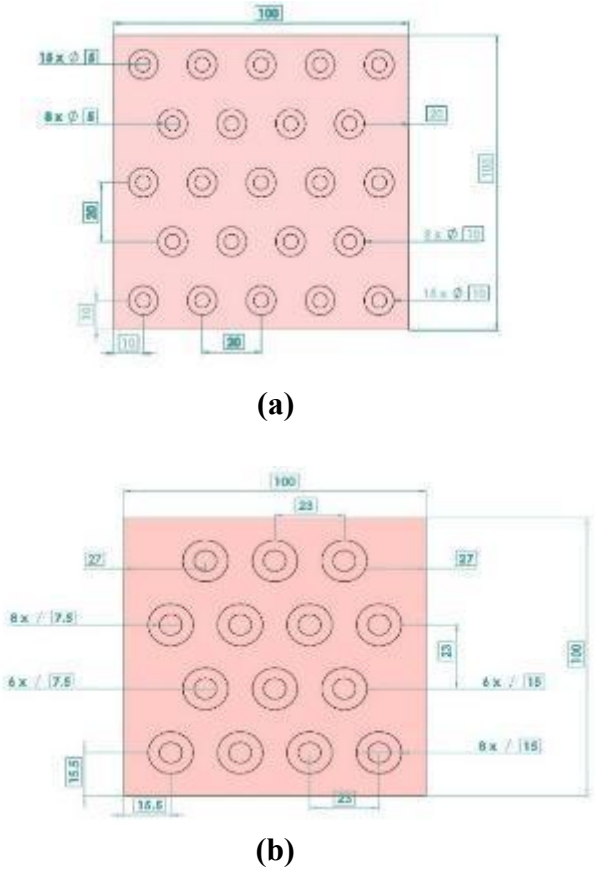


Fig. 6. Top-view schematic diagrams illustrating the fin dimensions, pitch spacing, and staggered layouts for: (a) the 10 mm series (23 pins), and (b) the 15 mm series (14 pins). All dimensions are in millimeters.

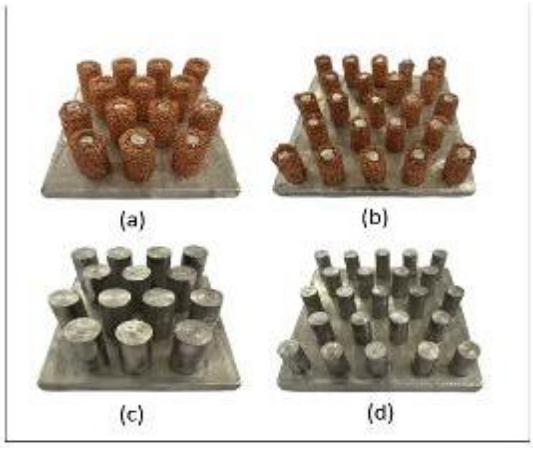


Fig. 7. (a, b) Hybrid aluminum–copper foam configurations and (c, d) baseline bare aluminum pin-fins for the 10 mm and 15 mm diameter series, respectively.

A copper metal foam with 90% porosity was selected to effectively balance thermal conductivity and aerodynamic permeability, as diagrammed in Fig. 8.



Fig. 8. Open-cell copper metal foam (ε = 90%) used for the hybrid fin encapsulation.

2.3. Material Properties

The thermophysical properties of all materials utilized in the experimental setup are summarized in Table 1**.** The fin cores and base plate were manufactured from aluminum alloy 6061 with a thermal conductivity of 167 W/m·K, adequate strength, and machinability.

The secondary heat transfer medium was high-purity open-cell copper foam whose skeletal thermal conductivity is much greater than that of aluminum (the bulk copper has ~400 W/m·K), enhancing the composite fin's effective conductivity.

The copper porous shell and aluminum structural core represent a high-performance solution to reduce the material cost and system mass compared to a monolithic copper construction, while sustaining superior convective properties provided by the copper ligament network.

The selected copper foam features a porosity (ε) of 90% and a pore density of 40 PPI (Pores Per Inch), corresponding to an average pore diameter of approximately 0.63 mm.

Based on established empirical models for open-cell metal foams, the estimated permeability (K) and inertial coefficient (CE) for this specific morphology are on the order of 5.5×10^{-8} m² and 0.09, respectively, which govern the aerodynamic resistance of the porous matrix.

Table 1: Thermophysical properties of the materials used in the experimental setup

Material	k (W/m.K)	ρ (kg/m3)	Cp (J/kg.K)
Al 6061	167	2700	896
Copper	400	8960	385
Kryonaut	12.5	-	-
Thermostone	0.15	600	1000

2.4. Experimental Procedure and Performance Metric

A total of 24 independent trials were conducted for all four heat sink configurations at two inlet velocities and three power levels. The main measure of performance was the steady-state temperature excess $\Delta T = Tb - Ta$. Here Tb is the spatially averaged base temperature and Ta is that of the inlet ambient. In order to quantify the comparative benefit arising from foam incorporation, a thermal enhancement ratio η (%) was defined as: [21],[22]

$$\eta\,(\%) = \left[\frac{(\Delta T_{bare} - \Delta T_{hybrid})}{\Delta T_{bare}}\right] \times 100 \qquad (1)$$

A positive η indicates that the foams lead to thermal enhancement with respect to the bare baseline, while a negative value indicates a thermal penalty due to foam-induced flow bypass.

To provide a clear overview of the experimental scope, the test variables are summarized in **Table 2**.

Table 2: Experimental Test Matrix

Parameter	Values
Heat Sink Geometries	Bare (PFHS), Hybrid (PFHS-MF)
Fin Outer Diameter (D)	10 mm, 15 mm
Inlet Air Velocity	0.75 m/s, 1.5 m/s
Applied Thermal Load	20 W, 40 W, 60 W

Measuring Procedure: For each test run, the centrifugal blower was first adjusted to the desired air velocity. Then, the electrical heater was turned on and set to the target power level.

The system was allowed to run until a steady-state condition was achieved (temperature variation ≤ ±0.1 °C for 10 minutes).

Finally, the transient and steady-state temperature data were recorded.

2.5. Uncertainty Analysis

The calibration specifications of each instrument were propagated as measurement uncertainty. Temperature readings exhibited a combined uncertainty of ±0.5 °C, airflow velocity readings a combined uncertainty of ±0.1 m/s, and the heater power was controlled at ±2%. Because the ΔT, the governing performance parameter, is the subtraction of two independent temperature measurements, the combined uncertainty equated to approximately ±1 °C.

The temperature trends discussed above are statistically significant relative to this measurement uncertainty.

For the 10 mm hybrid configuration at 0.75 m/s and 20 W, the temperature difference decreased from 40 °C to 34 °C (a change of 6 °C), which considerably exceeds the ±1 °C uncertainty limit. At a flow speed of 1.5 m/s and 60 W, this configuration exhibits a decrease in ΔT from 79 °C to 65 °C.

The 16 °C difference in thermal degradation, which exceeded that of the bare baseline for the 15 mm series, likewise falls well outside the measurement uncertainty, confirming that the bypass mechanism is a genuine physical effect.

Prior to the experiments, all measuring instruments were carefully calibrated to ensure data reliability. The Type-K thermocouples were calibrated against a standard precision thermometer in a constant-temperature water bath, yielding an accuracy of ±0.5 °C. The MT-4615 digital anemometer, used for velocity measurements, has a manufacturer-specified accuracy of ±0.1 m/s and was verified using a pitot-static tube setup. The electrical power supplied to the heater was regulated via a digital wattmeter with a control accuracy of ±2%.

Table 3: Specifications of the Measuring Instruments

Instrument	Model	Range	Accuracy
Thermocouples	Type-K	-200 to 1260 °C	±0.5 °C
Digital Anemometer	MT-4615	0.3 to 30 m/s	±0.1 m/s
Digital Wattmeter	Standard	0 to 1000 W	±2%

3. Results and Discussion

While fundamental dimensionless parameters such as the Nusselt number and convective heat transfer coefficient are valuable for theoretical fluid dynamics, the present study utilizes the steady-state temperature excess (ΔT) and the thermal enhancement ratio (η) as the primary performance metrics. In the context of applied electronic cooling, ΔT provides a direct, practical measure of the heat sink's ability to maintain junction temperatures within safe operational limits under specific power loads, which is the ultimate goal of thermal management systems.

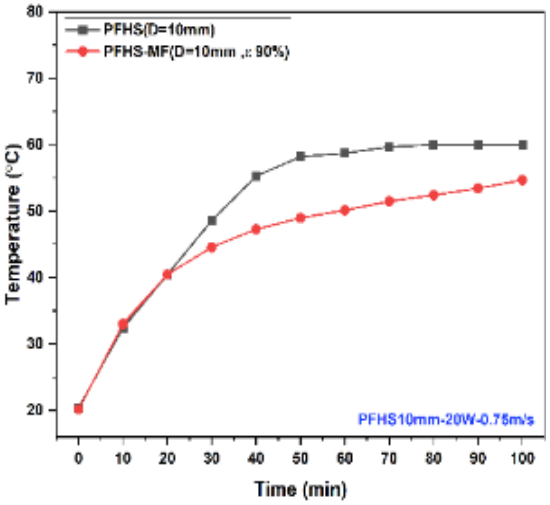
3.1. Thermal Performance of the 10 mm Series: Effect of Thermal Load

3.1.1. Thermal Response at 0.75 m/s

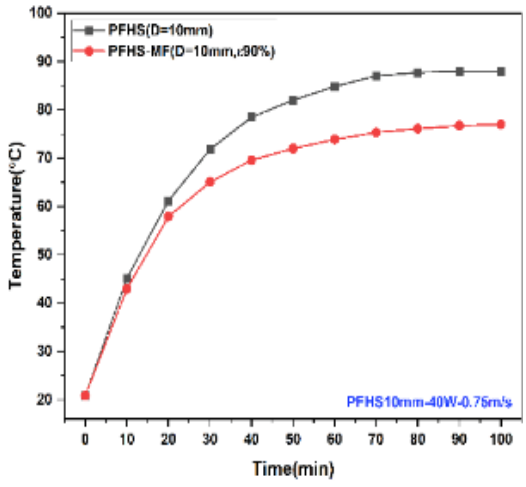
The steady-state and transient thermal characteristics of the bare pin-fin heat sink (PFHS) and the hybrid configuration (PFHS-MF) with 90% porosity for the 10 mm series at a constant airflow velocity of 0.75 m/s are shown in Fig. 9. The results were obtained under applied power levels of 20 W, 40 W, and 60 W, respectively. The foam-integrated design exhibits lower base temperatures than the bare configuration over the entire power range. As the applied power increases from 20 W to 60 W, the time taken to achieve steady state increases from 60 minutes to 90 minutes.

An analysis with the help of Equation (1) at all power levels in this speed range confirmed that foam encapsulation provides a thermal benefit. The hybrid configuration at 20 W decreases the steady-state base temperature from 60 °C to 54 °C (ΔT from 40 °C to 34 °C) that is η = 15.0%. At 40 W, the foam-wrapped design limits the base temperature to 77 °C, while a bare-fin peak reaches 88 °C, yielding η = 16.2 %. The hybrid configuration keeps the base at 108 °C against 120 °C of the bare array under the extreme load of 60 W, which implies η = 12.0%. Even when the 0.75 m/s air stream lacks sufficient momentum to fully penetrate the porous matrix, the copper foam still contributes by conduction: its highly conductive ligaments spread the heat laterally and radially across a greatly enlarged wetted surface area.

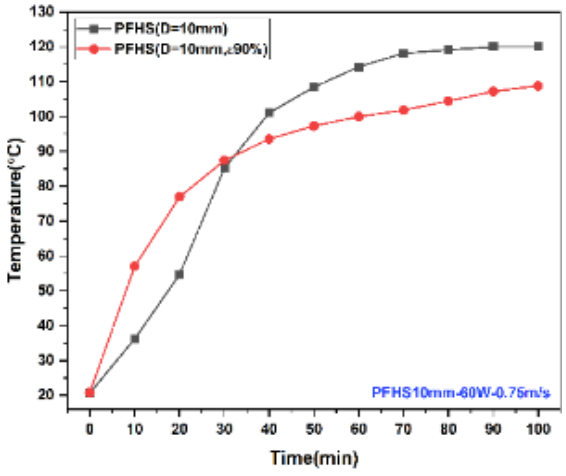
Physical Reasoning: As the applied thermal load increases, the heat flux at the base intensifies, which physically explains the upward trend in all temperature curves. However, the hybrid configuration maintains lower peak temperatures because the interconnected copper ligaments provide continuous conduction pathways. This effectively spreads the heat and increases the overall thermal inertia of the system, delaying the temperature rise compared to the bare aluminum fins.



(a)



(b)



(c)

Fig. 9. Comparative transient thermal response of bare PFHS and 90% porosity PFHS-MF (D = 10 mm) at a constant air velocity of 0.75 m/s under varying heat loads: (a) 20 W, (b) 40 W, and (c) 60 W.

3.1.2. Thermal Response at 1.5 m/s

The thermal features at 1.5 m/s inlet speed are presented in figures 10a-10c. As speed increases, there is a significant reduction in absolute base temperatures at all power levels.

This confirms that convective intensity is the dominant driver of thermal performance. Using equation (1): at 20 W (fig. 10a), the hybrid design reaches a steady-state temperature of 44 °C while the bare sink reaches 49 °C giving η = 17.2% (ΔT from 29 °C to 24 °C).

At a power output of 40 W (see Fig. 10b), the PFHS-MF limits the temperature of the base to 68 °C, whereas a bare peak reaches 75 °C, which corresponds to η = 12.7 %. When the input power is increased to 60 W (fig. 10c), the foam-wrapped configuration maintains the base at 85 °C, while the plain fins reach the maximum temperature of 99 °C.

The maximum enhancement measured for this configuration is η = 17.7%. The air stream at a velocity of 1.5 m/s has sufficient kinetic energy to overcome hydraulic resistance of 90% porosity copper-foam and penetrate within the interstitial voids which thins thermal boundary layers and sustains buoyant mixing.

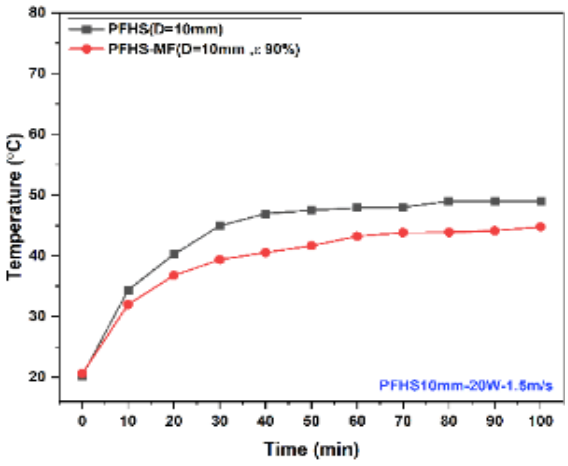
3.2. Thermal Performance of the 10 mm Series: Effect of Air Velocity

3.2.1. Velocity Sensitivity at 20 W

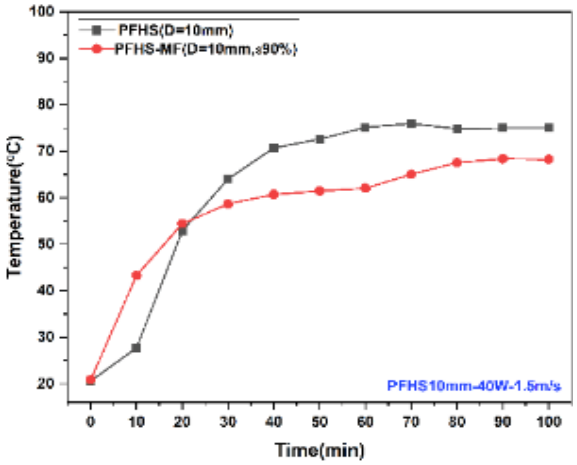
Thermal response comparison of 10 mm configurations at 20 W when inlet velocity is doubled from 0.75 m/s to 1.5 m/s in Figs. 11a and 11b. The steady-state temperature of the bare heat sink decreases from 60 °C to 49 °C, corresponding to a velocity-induced improvement of 27.5%.

The hybrid configuration shows a more favorable response too; the base temperature drops from 54 °C to 44 °C resulting in a velocity-induced gain of 29.4%, which is the largest single-variable improvement in the 10 mm series.

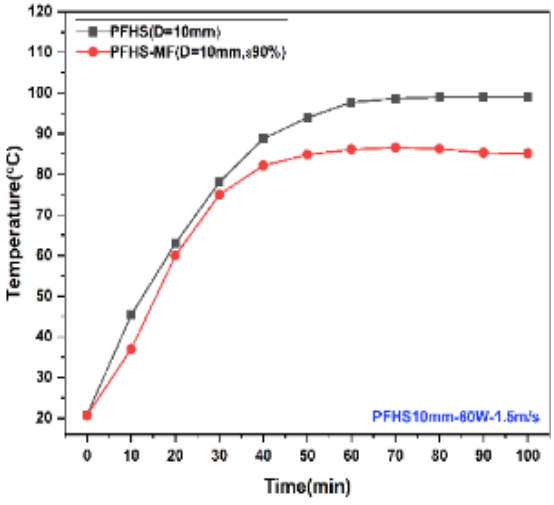
This increased sensitivity indicates that the higher-momentum flow more effectively exploits the tortuous architecture of the copper foam.



(a)



(b)



(c)

Fig. 10. Comparative transient thermal response of bare PFHS and 90% porosity PFHS-MF (D = 10 mm) at a constant high air velocity of 1.5 m/s under varying heat loads: (a) 20 W, (b) 40 W, and (c) 60 W.

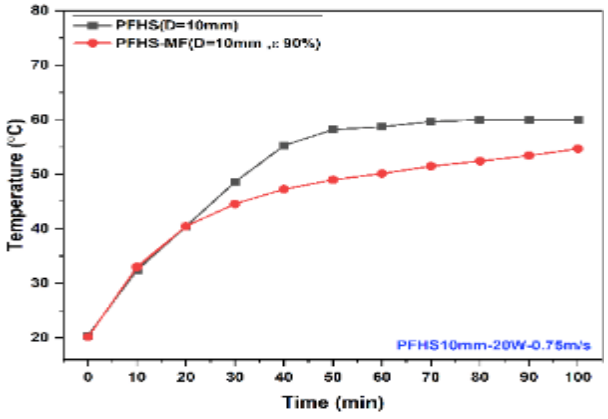
Physical Reasoning: The physical mechanism behind this significant temperature drop with increased velocity is attributed to the thinning of the thermal boundary layer around the solid fins and the porous ligaments. At a higher velocity (1.5 m/s), the increased mass flow rate of the air carries away more sensible heat. For the 10 mm hybrid configuration, the highly conductive copper foam acts as an effective extended surface. The tortuous nature of the pores disrupts the airflow, creating local micro-vortices and enhancing fluid mixing. This continuous replenishment of the cold fluid within the porous matrix significantly boosts the convective heat transfer rate, explaining the superior performance of the hybrid design over the bare fins.

3.2.2. Velocity Sensitivity at 40 W

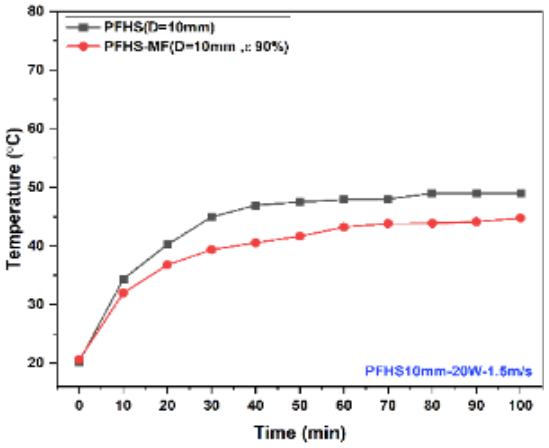
Doubling the speed results in a decrease in the bare-fin peak temperature from 88 °C to 75 °C at a power level of 40 W. The hybrid configuration exhibits a similar decrease, from 77 °C to 68 °C.

The thermal enhancement ratio η = 12.7% is sustained at two velocities, demonstrative of the fact that the foam-incorporated design, relative to other designs, maintains its superiority with increasing convective intensity.

At higher speeds, the air flow retains sufficient kinetic energy while crossing the porous matrix, which helps minimize the hot-spot formation that is more pronounced at lower flow rates.

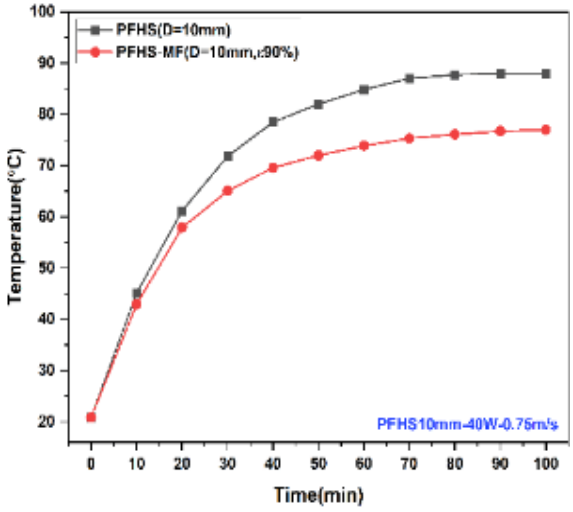


(a)

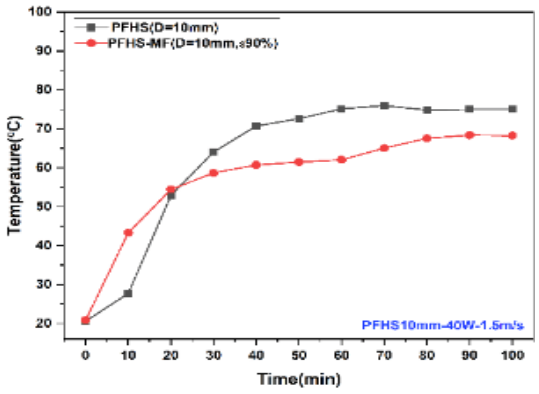


(b)

Fig. 11. Comparative transient and steady-state PFHS-MF at a constant moderate heat load of 20 W: (a) at 0.75 m/s, (b) at 1.5 m/s.



(a)

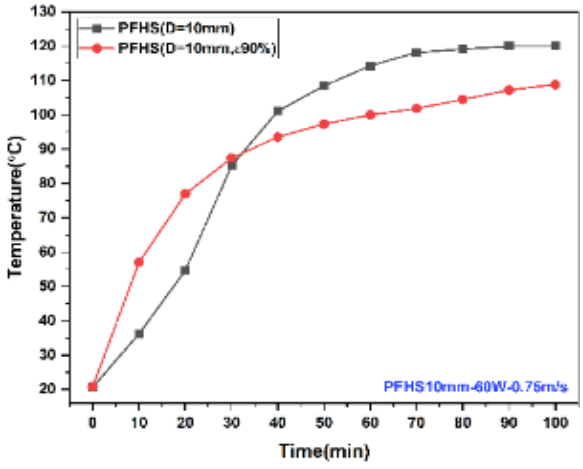


(b)

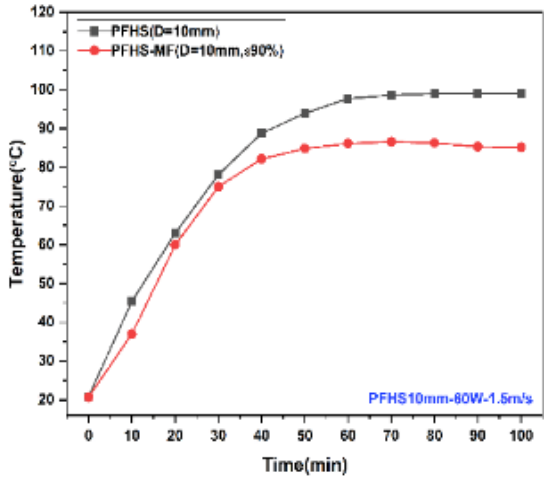
Fig. 12. Influence of inlet air velocity on the thermal stability of bare and hybrid heat sinks subjected to an intermediate heat load of 40 W: (a) at 0.75 m/s, (b) at 1.5 m/s.

3.2.3. Velocity Sensitivity at 60 W

The flow rate of 0.75 m/s is inadequate to prevent the bare configuration from crossing the 120 °C temperature mark under the highest thermal load of 60 W (Figs. 13 a, b). When the velocity is doubled to 1.5 m/s, the bare and hybrid configurations exhibit temperature decreases to 99 °C and 85 °C, respectively. For the hybrid design, that velocity increment means a cooling improvement of 26.1% (ΔT switch from 88 °C to 65 °C). At this condition the principal mechanism shifts from diffusion limited interstitial transport to advective dominated interstitial transport. High momentum air penetrates deep within the copper foam and provides maximum convective coefficient over the whole ligament surface.



(a)



(b)

Fig. 13. Thermal mitigation characteristics and peak temperature suppression of bare PFHS and 90% porosity PFHS-MF under severe thermal stress (60 W): (a) at 0.75 m/s, (b) at 1.5 m/s.

3.3. Thermal Performance of the 15 mm Series: Effect of Thermal Load

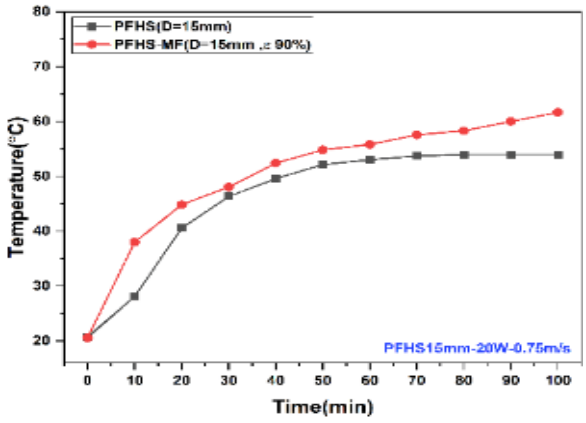
3.3.1. Thermal Response at 0.75 m/s

The transient and steady-state thermal characteristics obtained at 0.75 m/s for the 15 mm series (Figs. 14a–14c) indicates that they behave quite differently to the compact 10 mm family.

At 40 W (Fig. 14b), the temperature of the bare configuration stabilizes at 76 °C while that of the hybrid design reaches 79 °C, giving a negative enhancement ratio η = −5.3% (ΔT increases from 56 °C to 59 °C). This thermal inversion is caused by a macro-scale aerodynamic bypass mechanism, produced by the geometric characteristics of the 15 mm series.

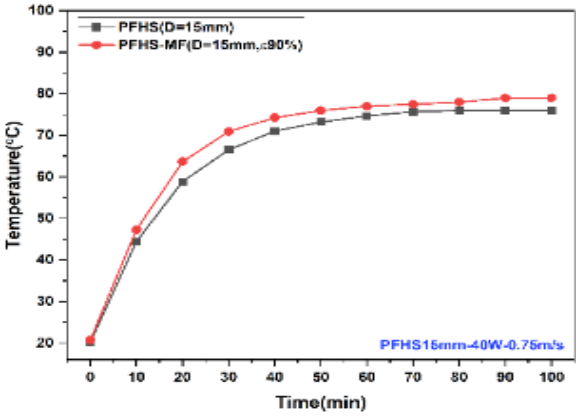
Although direct flow visualization and pressure drop measurements were not conducted in this study, the severe thermal degradation (η=−5.3%to −24.6%) provides strong indirect evidence of a macro-scale flow bypass. According to the principle of least flow resistance, fluid tends to follow the path of minimum hydraulic impedance. In the 15 mm series, the addition of the 2.5 mm thick foam sleeve significantly reduces the inter-fin clearance.

Consequently, the hydraulic resistance of the dense porous matrix exceeds the resistance of the open channels surrounding the heat sink array. This forces the oncoming air stream to divert around the heat sink rather than penetrating the foam, effectively starving the extended surfaces of the necessary coolant and leading to the observed thermal penalty.



(a)

At 0.75 m/s, the foam-coated fin geometry presents enough hydraulic resistance to provoke pronounced flow deviation: most of the incoming air is diverted around the edge of the heat sink array rather than penetrating the porous matrix, thereby shielding the foam-covered ligaments from convective cooling.



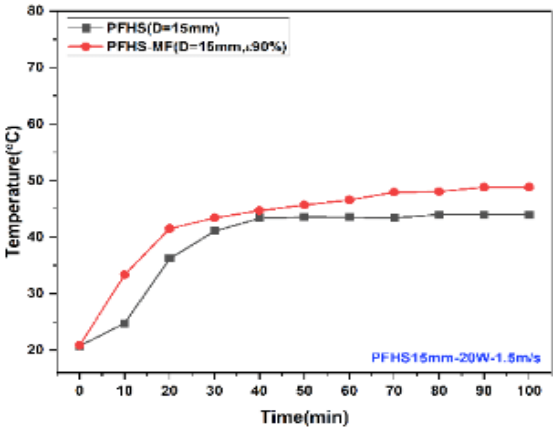
(b)

Fig. 14. Comparative transient thermal response of bare PFHS and 90% porosity PFHS-MF (D = 15 mm) at a constant air velocity of 0.75 m/s under varying heat loads: (a) 20 W, (b) 40 W, and (c) 60 W.

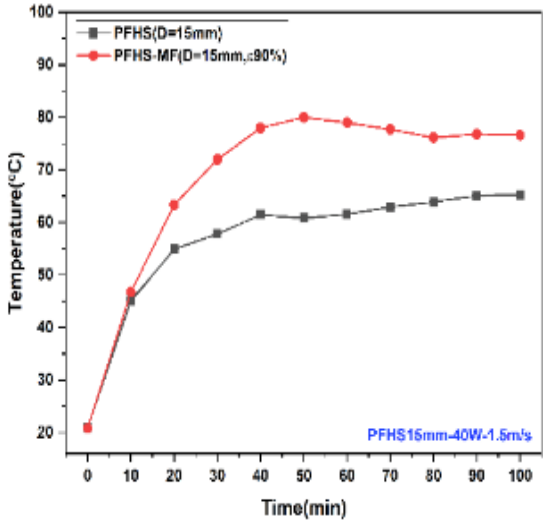
3.3.2. Thermal Response at 1.5 m/s

When the inlet velocity is increased to 1.5 m/s (Figs. 15a-15c), the absolute temperatures are lowered in both bare and hybrid 15 mm cases, but the performance drop for the foam case is still unrecovered. At maximum power of 60 W (Fig. 15c), the bare PFHS reaches a steady-state temperature of 85 °C whereas the PFHS−MF stabilizes at 101 °C corresponding to a large thermal penalty η = −24.6 % (ΔT increases from 65 °C to 81 °C). Although the stream of 1.5 m/s possesses greater kinetic energy, the highly constricted inter-fin clearances in the 15 mm foam-wrapped array continue to function as overriding aerodynamic blockages. The outcome mentioned above clearly illustrates that, beyond a certain geometry scale, the additional surface area contributed by the porous sheath is not adequate to overcome the strong reduction in aerodynamic permeability.

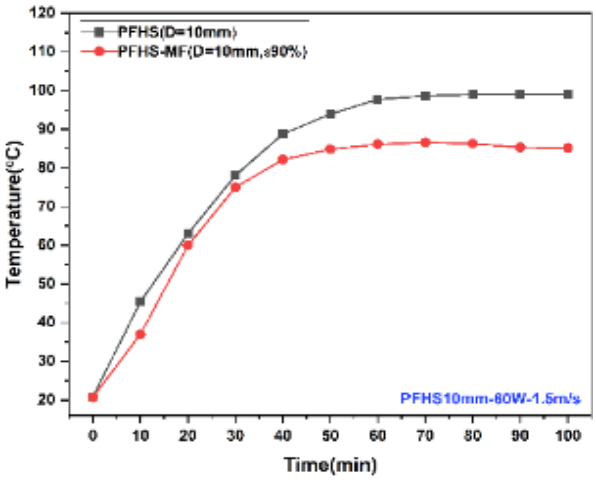
Physical Reasoning: From a physical perspective, the upward shift of the hybrid temperature curves above the bare baseline in these figures indicates a transition from advection-dominated heat transfer to conduction-dominated transfer. Because the incoming air bypasses the dense 15 mm array, the air trapped within the foam pores becomes stagnant. Since stagnant air has a very low thermal conductivity, the foam sleeve physically acts more as a thermal insulator rather than a convective enhancer, trapping the heat and causing the base temperature to rise sharply.



(a)



(b)



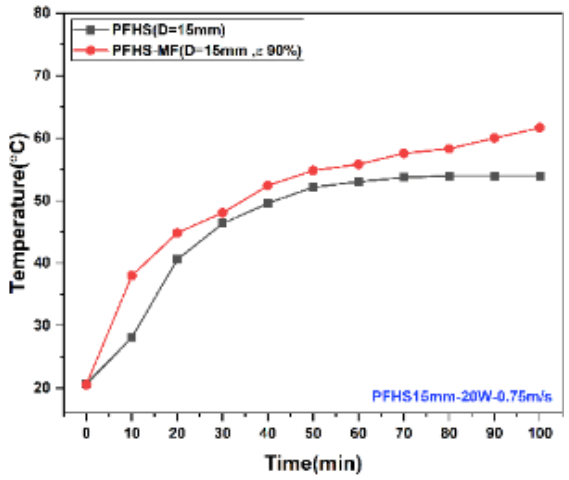
(c)

Fig. 15. Comparative transient thermal response of bare PFHS and 90% porosity PFHS-MF (D = 15 mm) at a constant high air velocity of 1.5 m/s under varying heat loads: (a) 20 W, (b) 40 W, and (c) 60 W.

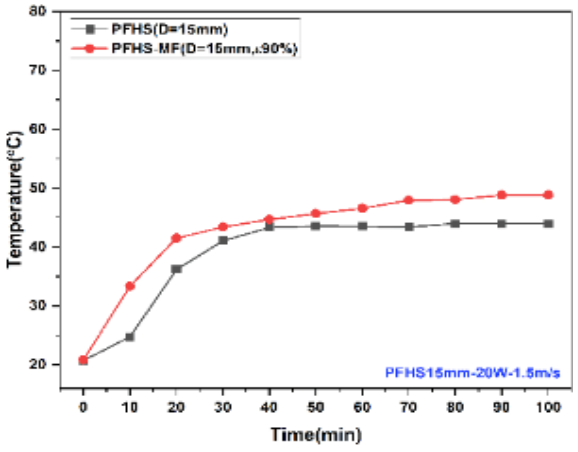
3.4. Thermal Performance of the 15 mm Series: Effect of Air Velocity

3.4.1. Velocity Sensitivity at 20 W

The velocity dependence at 20 W for the 15 mm series is shown in Figures 16a and 16b. Increase in inlet velocity from 0.75 m/s to 1.5 m/s could reduce the temperature in the case of hybrid configuration from 62 °C to 49 °C or a velocity induced improvement of 30.9% in temperature excess. The improvement at low power is comparatively modest, since the hydraulic resistance associated with 20 W still allows the approaching flow to penetrate sufficiently to interact with the outer ligament layer of the foam annulus.



(a)

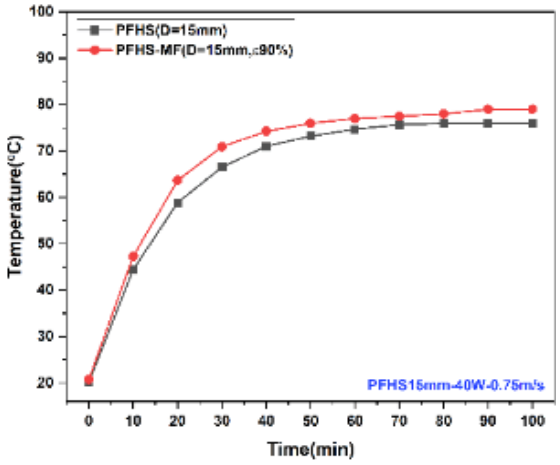


(b)

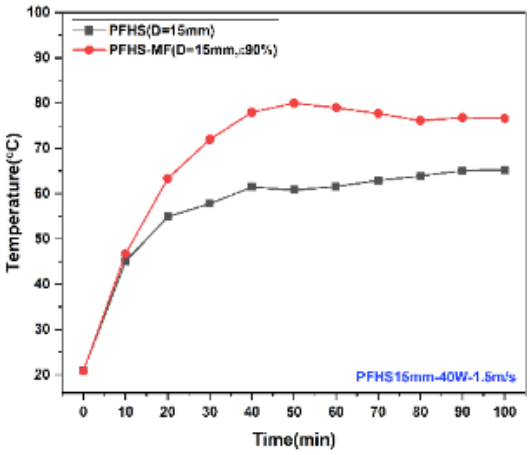
Fig. 16. Influence of inlet air velocity on the thermal stability of bare and hybrid heat sinks (D = 15 mm) at a constant load of 20 W: (a) 0.75 m/s, (b) 1.5 m/s.

3.4.2. Velocity Sensitivity at 40 W

At 40 W (Figs. 17a and 17b), the velocity is changed to yield 0.75 m/s at that of 1.5 m/s which results in a marginal 3.4% increase of the hybrid 15 mm setup (79 °C to 77 °C). The reduced sensitivity to flow velocities shows that the thermal load is now limited by the aerodynamic blockage of the larger foam-set fins, overpowering the increase in convective gains one would expect with a two-fold increase in flow velocities.



(a)

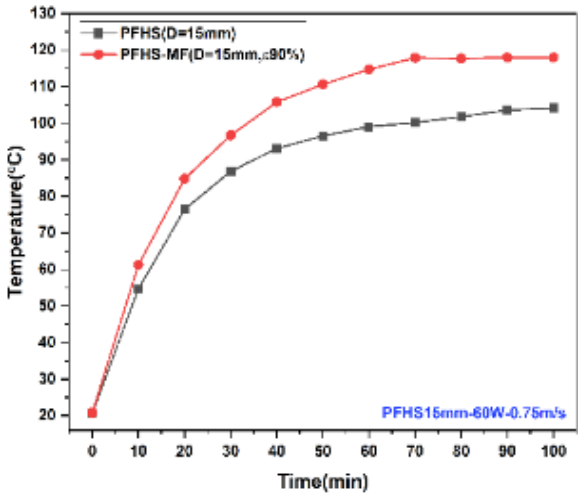


(b)

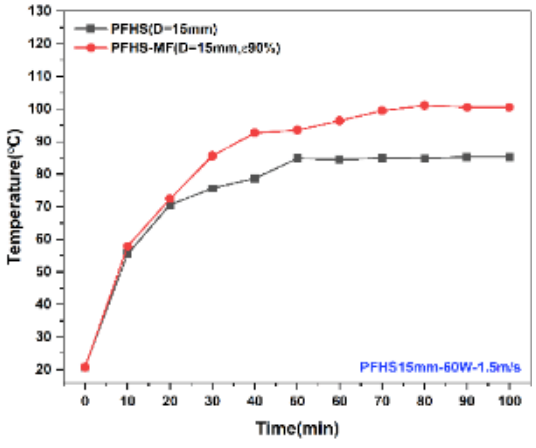
Fig. 17. Influence of inlet air velocity on the thermal stability of bare and hybrid heat sinks (D = 15 mm) at a constant load of 40 W: (a) 0.75 m/s, (b) 1.5 m/s.

3.4.3. Velocity Sensitivity at 60 W

At the maximum power of 60 W (Figs. 18a and 18b), the hybrid 15 mm configuration reaches a peak of 118 °C at the speed of 0.75 m/s. When the velocity was increased to 1.5 m/s, the base temperature recovered to 101 °C, corresponding to an improvement of 17.3%. While this is a significant reduction in absolute temperature, the negative enhancement ratio relative to the bare baseline shows that foam integration in the 15 mm series is a net thermal liability under all conditions tested. These results indicate that, for porous-augmented large-diameter fin configurations, increasing the forced-convection velocity alone is a necessary but insufficient corrective measure.



(a)



(b)

Fig. 18. Thermal mitigation characteristics of bare and hybrid heat sinks (D = 15 mm) under severe thermal stress (60 W): (a) 0.75 m/s, (b) 1.5 m/s.

Comparison with Previous Works and Practical Applications:

The maximum thermal enhancement of 22.5% achieved by the 10 mm hybrid configuration aligns well with, and in some cases exceeds, the enhancements reported in recent literature for solid-porous architectures (e.g., Ghaleh et al. [22] and Zohora et al. [33]), which typically range between 15% and 20% under steady-state conditions. However, the novelty here lies in demonstrating the transient stability of these hybrid sinks under varying loads. From a practical standpoint, these findings can be directly translated into the thermal management of high-density microelectronics, such as CPUs, GPUs, and power electronics. The ability of the 10 mm copper-foam encapsulation to suppress peak temperatures during transient power surges makes it highly suitable for devices subjected to variable and unpredictable workloads, ensuring their reliability and extending their operational lifespan.

Conclusion

This study systematically characterizes the steady-state and transient thermal performance of hybrid metal foam–pin fin heat sinks under forced convection. By isolating the effect of fin outer diameter, this work uniquely identifies the geometric threshold that dictates whether foam integration provides thermal enhancement or induces a detrimental flow bypass. The main findings and design guidelines are summarized as follows:

- **Thermal Enhancement:** The compact 10 mm hybrid design consistently outperformed the bare baseline, achieving a peak thermal enhancement ratio of 22.5% due to the extended surface area and promoted local fluid mixing.
- **The Bypass Penalty:** The extended 15 mm hybrid series exhibited thermal degradation, with a maximum penalty of −24.6% at 1.5 m/s and 60 W, caused by severe macro-scale flow bypass.
- **Velocity Sensitivity:** Increasing the inlet velocity from 0.75 to 1.5 m/s yielded up to a 29.4% cooling improvement for the 10 mm hybrid configuration.
- **Design Guidelines:** Foam encapsulation is highly recommended for compact fin arrays to suppress peak temperatures during transient power surges. However, it should be avoided in dense arrays (e.g., 15 mm) where insufficient inter-fin clearance leads to detrimental flow bypass.

Acknowledgements

The support provided by Northern Technical University and the Engineering Technical College of Mosul, Department of Power Mechanic Techniques Engineering, Iraq, in carrying out the experimental

work of this research is gratefully acknowledged by the authors.

Conflict of Interest

The authors declare that there is no conflict of interest regarding the publication of this work.

Data Availability Statement

The corresponding author will provide the raw data of the study upon reasonable written request. These data can be used to replicate the results.

References

[1] H. Rasam, P. Roy, L. Savoldi, and S. Ghahremanian, "Numerical assessment of heat transfer and entropy generation of a porous metal heat sink for electronic cooling applications," Energies, vol. 13, no. 15, p. 3851, 2020. https://doi.org/10.3390/en13153851

[2] Y. Fang, T. Liu, and D. Sun, "Research on novel thermal management technology in the field of integrated circuits," in Proc. 25th Int. Conf. Electronic Packaging Technology (ICEPT), 2024, pp. 1–6. https://doi.org/10.1109/ICEPT63120.2024.10668500

[3] A. S. Kurhade et al., "State-of-the-art cooling solutions for electronic devices operating in harsh conditions," J. Mines Metals Fuels, pp. 843–861, 2024. https://doi.org/10.18311/jmmf/2024/45374

[4] V. Kanate et al., "Numerical investigation on performance of CPU heat sinks," in Lecture Notes in Mechanical Engineering, 2024, pp. 361–372. https://doi.org/10.1007/978-981-99-7827-4_29

[5] Q. Wang et al., "Passive enhanced heat transfer, hotspot management and temperature uniformity enhancement of electronic devices by micro heat sinks: A review," Int. J. Heat Fluid Flow, vol. 107, p. 109368, 2024.

[6] L. Swetha, R. Parameshwaran, and S. S. Deshmukh, "Progress in thermal management of conventional to next-generation heat sinks using phase change materials: A review," J. Therm. Anal. Calorim., vol. 150, no. 24, pp. 20021–20046, 2025.

[7] Y. Janabi et al., "A review study of different effects on the performance of natural convection within enclosures," Int. J. Heat Technol., vol. 42, no. 3, pp. 1037–1057, 2024.

[8] O. Kosdere, Z. Sert, and O. Altun, "Investigation of thermal performance at forced convection in plate-fin heat sink," Energy, vol. 307, p. 132621, 2024.

[9] S. Wang et al., "Forced convection enhancing evaporative cooling of a sessile droplet," Phys. Fluids, vol. 37, no. 12, 2025.

[10] L. Zhong, W. Su, and Z. Shen, "Effect of varying Reynolds numbers on the heat transfer and flow structure of vertical, curved, inclined, and serpentine pin fins," Int. Commun. Heat Mass Transfer, vol. 161, p. 108557, 2024.

[11] F. Bunjaku, K. Buza, and R. V. Filkoski, "Comparative analysis of thermal performance and geometric characteristics of tubes with rectangular and triangular fins," Processes, vol. 13, no. 10, p. 3256, 2025.

[12] F. Zohora et al., "Optimization of hydrothermal performance in industrial heat sinks with innovative perforated pin fin designs: A numerical approach," Heliyon, vol. 11, no. 1, p. e41496, 2024.

[13] M. K. Sahu, P. Tiwari, and R. Giri, "Perforated pin fin design for improved heat transfer in thermal applications," AIP Conf. Proc., vol. 3389, p. 020023, 2026.

[14] A. Dixit, R. Maithani, and S. Sharma, "Effect of fin profile in a plate pin fin heat sink for performance enhancement," Exp. Heat Transfer, vol. 39, no. 3, pp. 219–242, 2025.

[15] Y. Chouksey, N. Shrivastava, and S. Kumar, "Performance evaluation of dovetail fin variants derived from a rectangular fin for laptop heat sinks," Int. J. Heat Fluid Flow, vol. 119, p. 110256, 2026.

[16] P. K. Singh, J. Joshi, and S. K. Sahu, "Experimental investigation of metal foam embedded surface thermal characteristics using air-jet impingement," Exp. Heat Transfer, vol. 38, no. 5, pp. 440–464, 2024.

[17] S. J. Kim et al., "A review of metal foam-enhanced pool boiling," Renew. Sustain. Energy Rev., vol. 210, p. 115176, 2024.

[18] P. V. Bansode et al., "Experimental analysis of heat transfer and pressure drop in aluminum metal foams immersed in dielectric synthetic fluid," in Proc. IEEE ITherm, 2024.

[19] K. K. Kumar and N. Sahoo, "Optimization of irreversibility factor with higher heat transfer rate in different pore density metal foams," Heat Mass Transfer, 2025.

[20] J. L. Torres-Madroñero et al., "Numerical analysis of non-regular and regular metal foam performance in heat transfer enhancing applications," Appl. Therm. Eng., vol. 273, p. 126562, 2025.

[21] H. A. Moghadam et al., "Parametric investigation of a solid-porous fin design for microchannel thermal performance improvement," Int. J. Heat Fluid Flow, vol. 118, p. 110210, 2025.

[22] M. S. Ghaleh et al., "Experimental and numerical analysis of porous metal foam effect on heat sink under impingement flow," Therm. Sci. Eng. Prog., vol. 67, p. 104156, 2025.

[23] M. Raje and A. K. Dhiman, "Effect of pore density and porosity of spiral porous metal fins for

waste heat extraction," Heat Transfer, vol. 55, no. 2, pp. 1155–1170, 2025.
[24] I. Issah et al., "Battery thermal management systems: From conventional approaches to hybrid configurations," Sustain. Mater. Technol., vol. 46, p. e01711, 2025.
[25] N. H. Roge, S. Krishnan, and S. Prabhu, "Thermal-hydraulic performance of partially filled stochastic metal foam heat sinks," Int. J. Therm. Sci., vol. 222, p. 110518, 2025.
[26] M. Al-Safadi et al., "CFD benchmarking of TPMS heat sink geometries," Int. Commun. Heat Mass Transfer, vol. 171, p. 110067, 2025.
[27] J. Shi, R. Zhu, and Z. Chen, "Pool boiling heat transfer mechanism on TPMS structures," Int. J. Heat Mass Transfer, vol. 261, p. 128574, 2026.
[28] V. A. Martinez, C. Caceres, and A. Ortega, "Experimental validation of effectiveness-NTU approach and thermal resistance definition," Int. J. Heat Mass Transfer, vol. 247, p. 127128, 2025.